The battle for silver binding: How the interplay between the SilE, SilF, and SilB proteins contributes to the silver efflux pump mechanism

Cyrielle Arrault, Yoan Rocky Monneau, Marie Martin, François-Xavier Cantrelle, Emmanuelle Boll, Fabien Chirot, Clothilde Comby Zerbino, Olivier Walker, Maggy Hologne

JBC RESEARCH ARTICLE

The battle for silver binding: How the interplay between the SilE, SilF, and SilB proteins contributes to the silver efflux pump mechanism

Received for publication, April 7, 2023, and in revised form, June 27, 2023 Published, Papers in Press, July 1, 2023,
https://doi.org/10.1016/j.jbc.2023.105004

Cyrielle Arrault[1,‡], Yoan Rocky Monneau[1,2,‡], Marie Martin[1], François-Xavier Cantrelle[3], Emmanuelle Boll[3], Fabien Chirot[4], Clothilde Comby Zerbino[4], Olivier Walker[1], and Maggy Hologne[1,*]

From the [1]Université de Lyon, CNRS, UCB Lyon1, Institut des Sciences Analytiques, UMR5280, Villeurbanne, France; [2]Department of Structural Biology, St Jude Children's Research Hospital, Memphis, Tennessee, USA; [3]Université de Lille, CNRS, UMR8576 – UGSF – Unité de Glycobiologie Structurale et Fonctionnelle, Lille, France; [4]Univ Lyon 1, Université Claude Bernard Lyon 1, CNRS, Institut Lumière Matière, UMR5306, Cité Lyonnaise de l'Environnement et de l'Analyse, Villeurbanne, France

Reviewed by members of the JBC Editorial Board. Edited by Wolfgang Peti

The resistance of gram-negative bacteria to silver ions is mediated by a silver efflux pump, which mainly relies on a tripartite efflux complex SilCBA, a metallochaperone SilF and an intrinsically disordered protein SilE. However, the precise mechanism by which silver ions are extruded from the cell and the different roles of SilB, SilF, and SilE remain poorly understood. To address these questions, we employed nuclear magnetic resonance and mass spectrometry to investigate the interplay between these proteins. We first solved the solution structures of SilF in its free and Ag^+-bound forms, and we demonstrated that SilB exhibits two silver binding sites in its N and C termini. Conversely to the homologous Cus system, we determined that SilF and SilB interact without the presence of silver ions and that the rate of silver dissociation is eight times faster when SilF is bound to SilB, indicating the formation of a SilF–Ag–SilB intermediate complex. Finally, we have shown that SilE does not bind to either SilF or SilB, regardless of the presence or absence of silver ions, further corroborating that it merely acts as a regulator that prevents the cell from being overloaded with silver. Collectively, we have provided further insights into protein interactions within the sil system that contribute to bacterial resistance to silver ions.

In the mid-20th century, the mass production of antibiotics emerged as a promising weapon to fight bacterial infections and has been massively used, unfortunately leading to the development of further antimicrobial resistance. As a result, there has been renewed interest in the use of silver for its antimicrobial properties (1). Silver is currently found in many everyday devices, such as silver-based wound patches, cosmetics, sanitary towels, or shower gels. More recently, it has been shown that silver enhances the antibacterial efficacy of clinically approved drugs as well as antibiotics (2, 3). However, similarly to antibiotic resistance, gram-negative bacteria have developed different resistance mechanisms to counteract the toxic effect of silver. This effect was first characterized in a strain of *Salmonella typhimurium* that caused the death of several patients in a burn unit in 1975 (4), and the genes responsible for silver resistance were ascribed to the plasmid pMG101 and designated the sil operon. Although the molecular mechanisms behind silver resistance still constitute an unsolved conundrum, the molecular basis has been reported in the seminal paper of Gupta *et al.* in 1999 (5). This mechanism is based on the expression of an efficient efflux transporter that expels metal ions out of the cell where the main key players are a tripartite efflux complex SilCBA, a small periplasmic metallochaperone SilF and a disordered SilE protein. SilCBA comprises an inner membrane transporter (SilA), an outer membrane protein (SilC), and a periplasmic protein (SilB). The deletion of *silc*, *sila*, *silb*, or *sile* results in a complete loss of resistance, while the deletion of the *silf* gene led to cell death when *cus* genes were also deleted (6).

It is thus an ongoing challenge to disentangle the functional mechanism of action that governs silver resistance and the corresponding interplay between SilCBA, SilF, and SilE of *S. typhimurium*. At present, only a few proteins of the sil system have been characterized, including SilE of *S. typhimurium* (7) and SilB from *Cupriavidus metallidurans* CH34, for which the structure and dynamics of its N- and C-terminus region, with and without silver, have been investigated (8, 9). While the C terminus folds into a SilF-like domain and binds silver ions (8), its N-terminus region is structured in solution and binds a silver ion that is caught between three conserved methionines (9). However, the sequence related to SilB of *S. typhimurium* displays only a low 28% identity with SilB of *C. metallidurans* CH34. Moreover, the latter one possesses a C terminus that is absent in the sequence of SilB from *S. typhimurium*. On the other hand, the CusFCBA system, which is orthologous to SilFCBA, has been more extensively studied, and CusF binds either Cu(I) or Ag(I) without significant structural changes. In the CusF apo form, Cu(I) or Ag(I) ions are coordinated by two methionines and one histidine and are further stabilized by a cation-π interaction due to a tryptophan (10, 11). Heavy-metal efflux by CusABC is driven by proton import, and this process

‡ These authors contributed equally to this work.
* For correspondence: Maggy Hologne, maggy.hologne@univ-lyon1.fr.

is catalyzed through the inner-membrane transporter CusA. The CusA structures suggest that the metal binding sites, formed by a three-methionine cluster, are located within the cleft region of the periplasmic domain (12). The metal binding triggers significant conformational changes and suggests a metal export through a channel of methionines, and very recently, four different conformations of CusA were identified and confirmed that CusA assembles as symmetric trimers where each of them can bind metal ions (13). CusB, which is the periplasmic protein of the tripartite heavy-metal efflux pump CusCBA, comprises four different domains where the first three domains are mostly β-strands. CusB can also interact with Cu(I) or Ag(I) ions through its N terminus which is essential for metal binding and transfer to CusF. Metal ions have been shown to interact with CusB and are maintained in place through a triad of methionines (14) which mutations result in a loss of metal binding (15). In an effort to understand the mechanism by which the efflux pump expels metal out of the cell, previous studies have demonstrated that CusF can transfer metal ions to the N terminus of CusB when one is at least in the apo form (16) prior to further relocation in CusA through a channel of methionines (12). Binding events occur through a multistep process that involves the initial formation of one or more CusF–CusB intramolecular complexes and lead to an intermediate that involves the metal coordinated by ligands belonging to both proteins (17).

In the present paper, we have solved the solution structures of SilF in its free and Ag-bound forms. In the Ag-bound form, we found that SilF binds silver through a set of residues that includes two methionines and one histidine, similarly to CusF. We have also characterized the Ag-bound form of SilB and identified two binding sites located at the N and C termini. While the interacting C terminus exhibits fast exchange rates, the Ag-bound N terminus displays NMR signals in slow to intermediate exchange and attests to the presence of conformational exchange. Conversely to what has been observed for the cus system, SilF and SilB interact even in the absence of silver ions. Importantly, the dissociation rate of silver ions from SilF is eight times faster when SilB is present, indicating a quick relocation of silver ions to form a shared binding intermediate SilF–Ag–SilB. Moreover, we have shown that SilE does not interact neither with SilF nor SilB, even in the presence of silver ions, ruling out a mechanism where SilE would act as a relay protein to further transfer silver to SilF prior to usher silver through SilB and SilA.

Results

Solution structure of SilF

The SilF construct used in this study comprises of 96 residues, with the first four residues not belonging to the SilF sequence (see Fig. S1 for the sequence numbering used in this study). The ^{1}H-^{15}N heteronuclear single quantum coherence (HSQC) spectrum exhibits 96 well-resolved backbone amide signals (Fig. S2*A*). NMR signals of most of the spin system were assigned, except for the first two residues in the N-terminal extension. The structure was solved based on the collection of an ensemble of 1787 nuclear overhauser effects (NOEs). The solution structure of SilF was determined using distance, torsional, and orientational constraints, as detailed in Experimental Procedures (Table S1).

The first 21 residues are highly flexible and did not show any inter-residue NOE correlations. This is in good agreement with the spin relaxation measurements (Fig. S3) that exhibit a strong decrease of the transverse relaxation rate in this region. From 22nd to 96th residues, the protein adopts a small β-barrel shape composed by five β-strands and capped by either a small α-helix of 1.5 step in one side and a 10-residues loop (loop 2) in the other side (Fig. 1*A*). The latter has a well-defined conformation based on its high number of long-range NOEs and their relaxation rates (Fig. S3). The sequence alignment with its two homologues gives a percent identity of 55% for *Escherichia coli* copper-binding protein CusF (Uniprot P77214) and only 36% for the metallochaperone domain of the *C. metallidurans* SilB (Uniprot Q581F3) (Fig. S4*A*). Nevertheless, the 3D structure of SilF is similar to the structures of those two homologues, the metallochaperone domain of SilB (Protein Data Bank [PDB] id. 2L55) and the copper-binding protein CusF (PDB id. 1ZEQ) (Fig. S4*B*). The root mean square deviations (RMSDs) (Cα atoms of the folded part of each protein) are 0.653 and 0.725 Å for the SilB domain and CusF respectively (Fig. S4*B*). The electronic doublet of the M53 sulfur is exposed to the solvent (M33 and M47 for CusF and SilB domain), making it accessible to bind to any silver ion in their vicinity. This conformation is confirmed by the presence of NOEs between the ε-methyl of M53 and both W50-Hα/Hβ and P51-Hδ. Interestingly, the H42 displays a H-bond between the imidazole hydrogen Hδ1 and the carbonyl of E43. This H-bond stabilizes the tautomer of H42, making the doublet of its Nε2 fully accessible but also holding the imidazole ring in a proper conformation to coordinate the Ag^{+} ion (Fig. 1*B*). The most divergent part of the proteins is the bottom of the β-barrel since we observed a small α-helix for SilF where only a loop was reported for CusF and the metallochaperone domain of SilB (Fig. S4*B*).

Solution structure of Ag-bound SilF (1:1)

The assignments of the Ag-bound SilF amide protons are displayed in Fig. S2*B*. The structure was solved based on the collection of an ensemble of 3402 NOEs. The solution structure of Ag-bound SilF was determined based on the distance, torsional, and orientational constraints, as detailed in Experimental Procedures (Table S2).

The structure of the bound state of SilF is very similar to the free state and the RMSD (Cα atoms of the folded part of each protein) is 0.50 Å (Fig. 1*C*). Here, the interaction of silver ions with the imidazole electronic doublet of the H42 induces a slight structural change in loop 2. Additionally, the 10 residues of the loop shift by 1 to 2 Å and the M53 rotates along its Cγ-Sδ bond (Fig. 1*C*). According to the crystal structure of Ag^{+}-CusF (PDB id. 2VB3), we defined the coordination of Ag^{+} to be planar and to involve the three electronic doublets of

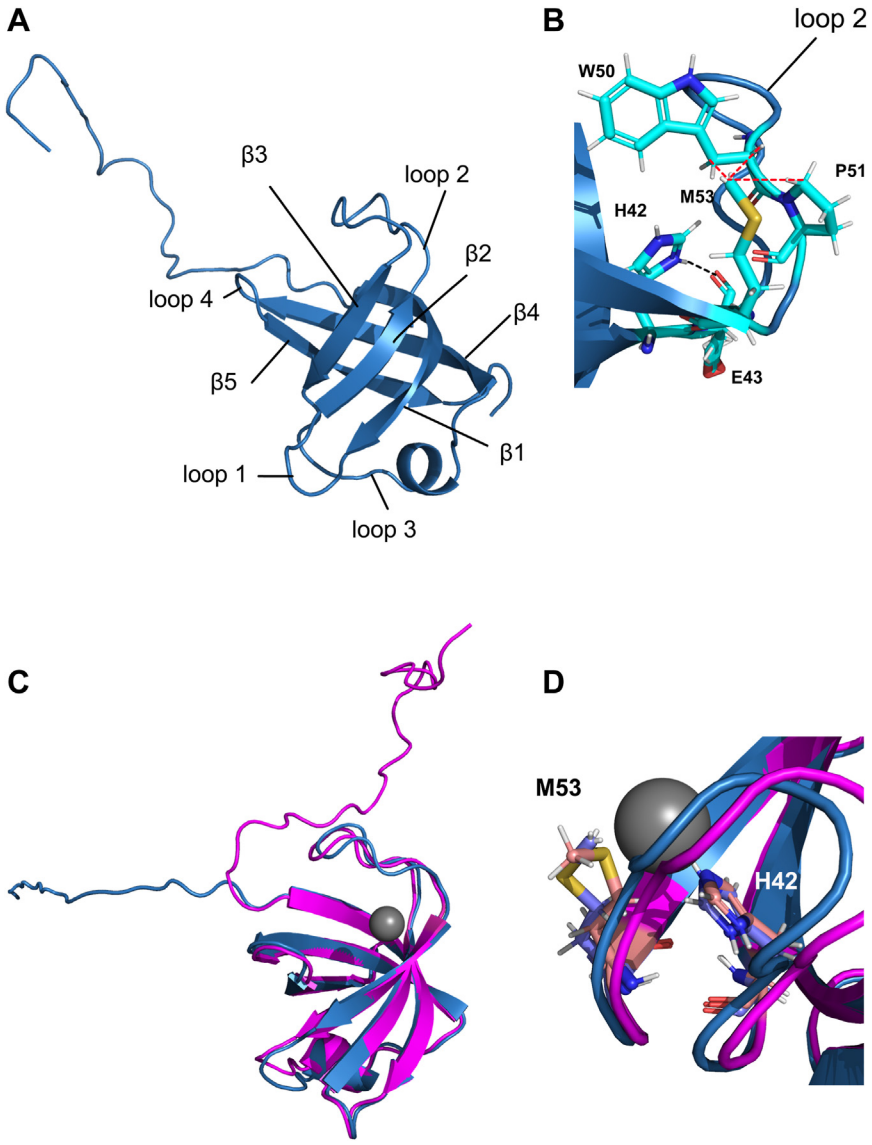

Figure 1. Solution structure of SilF and Ag-bound SilF (1:1). *A*, NMR-derived solution structure of SilF (structure one among 20 NMR-derived structures) along with the loops and β-strands numbering. *B*, magnified view showing the key residues of SilF loop 2. The NOEs between the ε-methyl of M53 and both W50-Hα/Hβ and P51-Hδ are displayed in *red dashed lines*, and the H-bond between Hδ1 of H42 and the carbonyl of E43 is displayed in *black*. *C*, comparison of the NMR-derived structure of SilF (*blue*) and Ag^+-SilF (*magenta*). *D*, zoom around residues M53 and H42. Note the rotation along the Cγ-Sδ bond of M53 for the Ag^+-SilF structure with respect to the SilF structure. NOE, nuclear overhauser effect.

M53-Sδ, M55-Sδ and H42-Nε2. This coordination pattern is further confirmed by the large chemical shift perturbations (CSPs) experienced by the M53 and M55 ε-methyl (16.8–18.8 ppm and 16.4–21.9 ppm respectively) and the Cδ2 of H42 in presence of silver ion (from 120 to 129.5 ppm). The RMSD between Ag^+-bound SilF and CusF is 0.57 Å (Fig. S5). The same rotation of M47 (analog of M53 in SilF) along its Cγ -Sδ bond is observed between the free and the silver-bound forms (Fig. 1*D*). As can be seen, the general fold is conserved and is comparable to the resulting tertiary structure of Cu-bound CusF (11) and Ag-bound CusF (10) (Fig. S5).

Silver binding to SilF

To investigate the interaction of SilF with silver ions, we monitored the CSPs in HSQC spectrum of a ^{15}N-labeled SilF sample upon addition of a solution of silver salt ($AgNO_3$). Upon titration, several SilF residues were affected and showed significant CSPs (Figs. 2 and S6). These residues are located on β-strands 1 and 2 and the connecting loop 2 and comprise hydrophobic (A44, I45, W50, M53) or charged residues (H42, E43, R56). Overall, the region affected by silver binding is consistent with the one found in its CusF counterpart in the Cus system where the conserved residues H36, M47, M49, and W44 (corresponding to H42, M53, M55, and W50 in SilF) are involved in copper or silver binding (11, 18).

Since no significant structural changes have been noticed upon silver binding, it is likely that the perturbations seen on the $^{1}H,^{15}N$ HSQC spectra solely result from the interaction with silver ions. A closer inspection of the $^{1}H,^{15}N$ HSQC spectra reveals that the residues involved in the interaction clearly exhibit a slow exchange regime with two separated resonances for the free and bound states (Fig. S6, *B* and *C*).

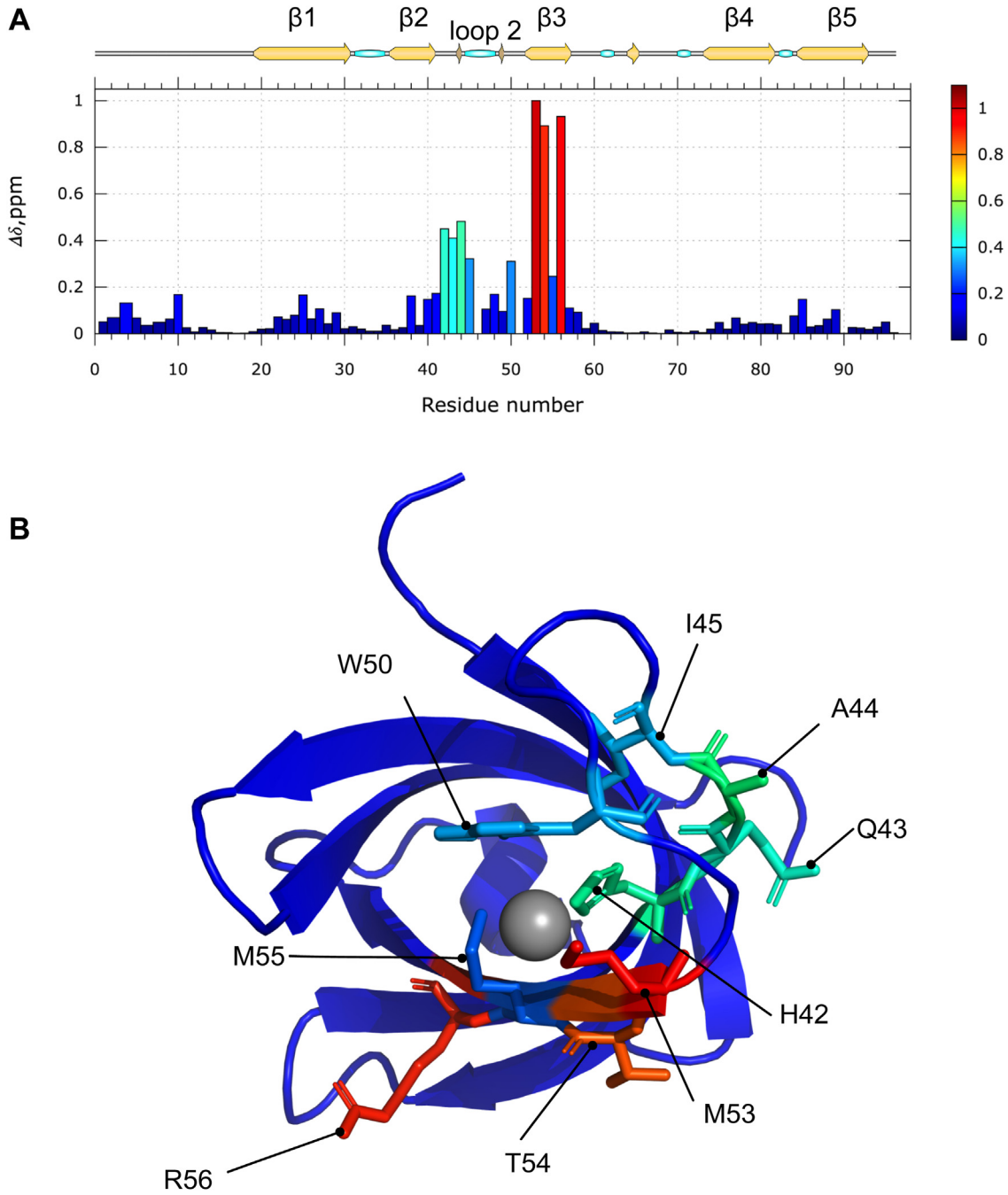

Figure 2. NMR characterization of the Ag^+/SilF interaction. *A*, CSPs (Δδ) for ^{15}N-SilF in the presence of one equivalent of silver ions as a function of residue number. The color palette highlights the largest CSPs (from *blue* to *red*). *B*, the observed CSPs in (*A*) are mapped onto the solution structure of SilF, including one silver (*gray sphere*). The same color palette is used as defined in (*A*). CSP, chemical shift perturbation.

NMR line shapes were analyzed by means of TITAN (19) to derive a dissociation constant (K_d) of 9.5 ± 3.5 μM and a dissociation rate (k_{off}) of 25.4 ± 4.5 s^{-1}. The errors were obtained by a Jackknife method implemented in TITAN software.

Silver binding to SilB

The SilB construct used here is composed of 406 residues, of which the first four residues do not belong to the SilB sequence (sequence numbering in Fig. S7*A*). The sequence alignment of SilB with its two homologues gives a percent identity of 67% for the *E. coli* copper-binding protein CusB (Uniprot P77239) and only 36% for the *C. metallidurans* SilB (Uniprot Q58AF3) (Fig. S7*B*). To investigate the interaction of silver ions with the 45 kDa ^{2}H,^{15}N-SilB sample, we used a ^{1}H-^{15}N transverse relaxation-optimized spectroscopy (TROSY)-HSQC experiment. Upon addition of 1 to 4 equivalents of silver ions to SilB, we observed significant CSPs, strong signal attenuation, or the presence of two resonances in conformational exchange of a limited number of signals. To avoid the long process of signal assignment and identify the affected residues, we first engineered a SilB1 construct

(21 kDa) comprising the membrane proximal domain and the N- and C-terminal flexible edges of SilB, as defined by the following sequence: ^{28}QL^{112}-G-^{329}SH^{430}. As seen on Fig. S8, the ^{1}H-^{15}N TROSY-HSQC spectra of ^{2}H,^{15}N-SilB and ^{2}H,^{15}N-SilB1 nicely overlap, demonstrating that they both share the same secondary and tertiary structure. To further validate our approach, we carried out NMR titration experiments on a ^{1}H,^{15}N-SilB1 sample and gradually added silver ions to reach a final ratio [Ag^{+}]/[SilB1] of 4 (Fig. S9*A*). The SilB1-affected residues were identical to those affected on SilB, attesting for the feasibility of our method. Most of the SilB1 NMR signals were assigned (Fig. S9*B*) by means of classical 3D NMR experiments and further transferred on the SilB spectra to identify the residues that were affected by silver binding. After the addition of one equivalent of Ag^{+}, F69, M70, and D71 showed strong signal attenuation, whereas V48, L49, F50, M55, D58, T59, K60, D62, K63, G65, S67, M72, D73, and L74 displayed two different resonances (Figs. 3*A* and S9*C*), indicating the existence of two conformations in a slow exchange regime in presence of silver ions. This observation was confirmed by a ^{1}H-^{15}N HSQC EXSY experiment recorded for a mixing time of 200 ms (Fig. S9*D*) that presents the typical hallmark of exchanging conformations. To localize the SilB affected residues, we have built a model of SilB based on ColabFold (20), running the AlphaFold prediction protocol (21). The Alphafold model structure of SilB displays two short beta-sheets and one turn for residues L49 to Y78 (Fig. 3*B*). This area shows a predicted local distance difference test (plDDT) of approximately 80 for the rank1 model (Fig. S10) and thus corresponds to a generally correct backbone prediction (22). The presence of four proline residues (P54, P57, P64, and P68) may induce local conformational exchange and would explain the observation of two NMR resonances per residue when silver is present. Additionally, the three sulfur atoms of M55, M70, and M72 point in the direction of the interior of the cavity and may bind one silver ion (inset of Fig. 3*B*). After the addition of two equivalents of Ag^{+}, we observe CSPs for some other residues belonging to the C-terminus region: L403, E410, E413, N414, S415, M416, A418, S420, Q422, N425, M426, G429, and H430 (Fig. 3*A*). This last result is in perfect agreement with those

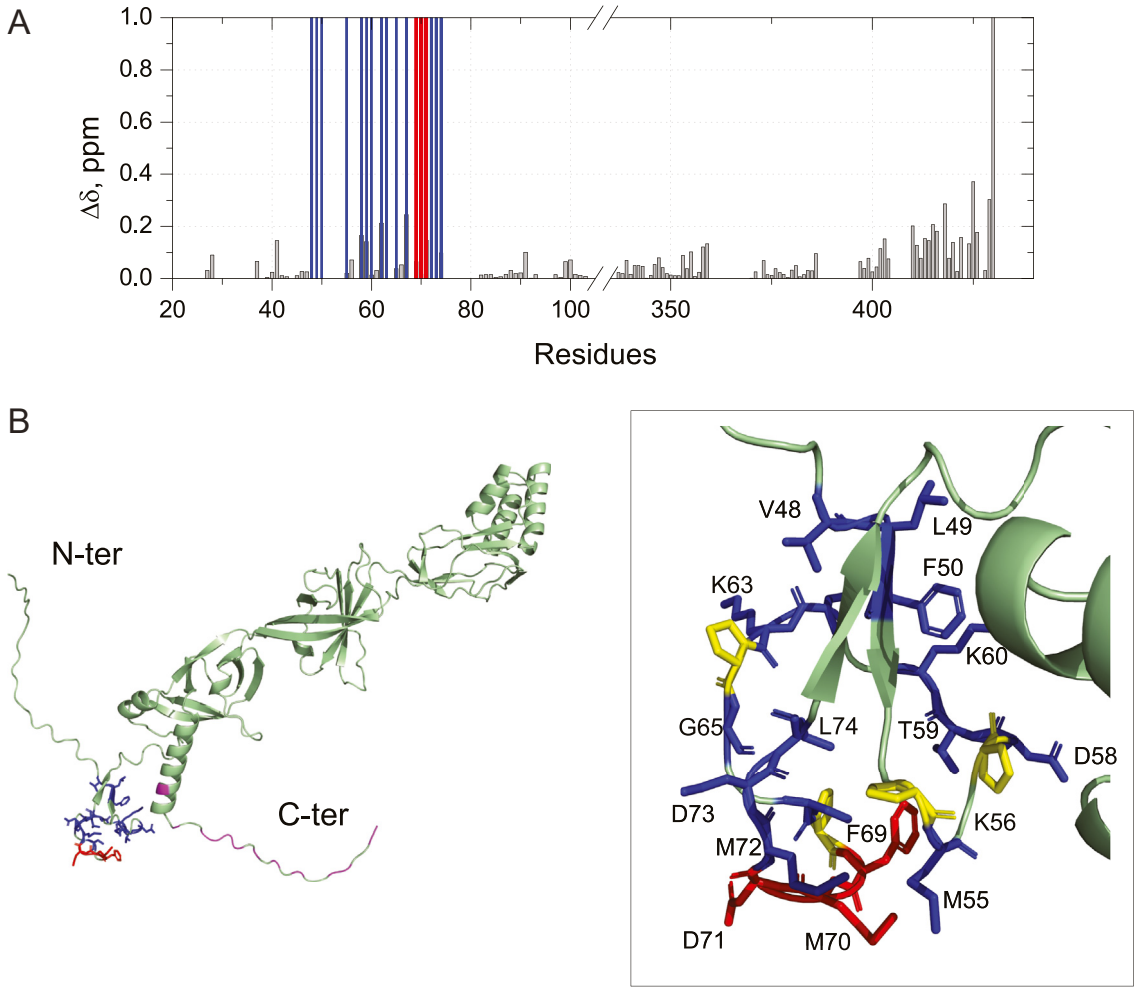

Figure 3. NMR characterization of the Ag^{+}/SilB interaction. *A*, CSPs (Δδ) for ^{15}N-SilB in the presence of four equivalents of silver ions as a function of residue number. The *blue bars* indicate residues that exhibit two resonances per residue in presence of *silver*, while the *red bars* refer to signals that disappear after the addition of 1eq. of Ag^{+}. *B*, Alphafold model prediction showing the 3D structure of SilB. The N-terminus binding site is represented with the colors (*red* and *blue*) defined in (*A*), while the C-terminus binding site is colored in *magenta*. The insert represents the N-terminus binding site along with its perturbed residues. Proline residues are displayed in *sticks* colored in *yellow*. CSP, chemical shift perturbation.

previously published by Babel *et al.* (23). Therefore, SilB harbors two different binding sites, the first one in the region encompassing residues M55 to F73, and the second one in the highly flexible C-terminus region.

SilF interacts with SilB without the presence of silver

Previous studies have reported that CusF and CusB homologous system only interact in the presence of silver (24). Therefore, we sought to understand whether SilF and SilB adopt a similar behavior. On a ^{15}N-SilF sample, we added an unlabeled sample of SilB at a [SilF]/[SilB] ratio of 1. As can be seen on Fig. S11*A*, the resulting ^{15}N-SilF HSQC spectrum shows significant signal shifts in fast exchange upon addition of SilB, indicating a direct and specific interaction of those proteins. Several observations can be drawn: first and foremost, the affected residues pattern differs from the one seen for the SilF/Ag^+ interaction. Indeed, extra residues located along β4 and β5 sheets exhibit CSPs (Fig. 4, *A* and *B*) and extend the SilF binding interface. It involves Q81, Q82, N84, I85, and S86. Second, the perturbed signals show weaker CSPs and different directions of the shifts compared to the SilF/Ag^+ interaction. The direction of the shifts of the ^{1}H-^{15}N signals reflects the ratio of ^{1}H and ^{15}N CSPs, which is unique for each residue (N-H bond) and for the changes in its electronic environment induced by binding. Thus, a change in the directions of the NMR signal shifts indicates a difference in the local intermolecular contacts, further supporting a model where SilF interacts with SilB with a different binding mode compared to the SilF/Ag^+ interaction. To confirm the SilF/SilB binding, we recorded two ^{1}H-^{15}N TROSY-HSQC spectra of a ^{2}H,^{15}N-SilB sample with or without unlabeled SilF at a [SilF]/[SilB] ratio of 1. As seen in Fig. 4, *C* and *D*, residues that encompass a region between M55 and L74 are significantly affected and correspond to the first site of silver binding that was previously described. The observation of a clear interaction between SilF and SilB without silver is in stark contrast compared to the cus system (16). Indeed, the alignment sequence shown in Fig. S7*B* highlights the fact that the perturbed residues K56 and K60 in SilB are replaced by Y50 and R54, respectively, in *E. Coli* CusB (Uniprot 77,234, Fig. S7*B*). In particular, the presence of Y50 in place of K56 may disrupt the interaction due to its hydrophobic nature in close proximity of W50 of SilF in the complex (Fig. 5*C*). Additionally, our NMR data are supported by the MALDI mass spectra (Fig. 5*A*) recorded for an equimolar mixture of SilF and SilB, that clearly display series of peaks at m/z 55,650 and m/z 27,825, consistent with 1:1 SilF/SilB complex singly charged and doubly charged, respectively. To gain insight into the structural organization of the SilF/SilB complex, we used the ColabFold multimer prediction tool (20). Surprisingly, without any prior knowledge, the predicted structure displays a contact surface that involves the most perturbed residues of both SilB and SilF when mixed at a 1:1 ratio. A closer look at the binding interface reveals that the residues M55, M70, D71, and M72 of SilB are in proximity with the residues W50, M53, M55, R56, and N84 of SilF (Fig. 5, *B* and *C*). Moreover, the interacting structures have a plDDT above 80, indicating that the predicted backbone structure is confident (Fig. S12).

Estimation of the bound fraction of the SilF/SilB complex

As reported earlier for the CusF–Ag–CusB complex, the measurement of spin relaxation was used to quantify the bound fraction of the complex (24). This hypothesis is valid, assuming that the order parameter (S^2), the global molecular tumbling and the anisotropy is kept similar in the free and in the bound form. In the present case, this hypothesis has to be ruled out due to several inconsistency listed hereafter: (i) the molecular shape of the SilF/SilB complex is far from being spherical but rather prolate and therefore induces a clear anisotropy of the diffusion tensor. The resulting relaxation parameters may significantly deviate from their isotropic behavior (see Fig. S13*B* in case of significant anisotropy) and (ii) the N-terminus domain of SilB that interacts with SilF is a small domain that is separated from the rest of the protein by a highly flexible linker. As we have previously demonstrated, such a flexibility induces a strong modification of the relaxation parameters (25). Each of the domains have their own, different correlation times so that the SilB protein could not be considered as a unique spherical protein. Consequently, when SilF binds SilB, the ^{15}N-SilF relaxation parameters will reflect the rotational tumbling associated with SilF and the N terminus of SilB and not the whole SilB. Experimentally, the average R_1 and R_2 values calculated over the range of well-structured residues of SilF for the SilF/SilB complex give 1.47 ± 0.12 and 19.8 ± 2.0 s^{-1}, respectively (Table 1 and Fig. S13*A*). These values significantly deviate from their expected values if the shape of the complex would be spherical but rather reflect the molecular weight of the SilF and the N terminus of SilB, as expected (Fig. S13*B*). This statement is corroborated by our theoretical prediction of the relaxation parameters for the SilF/SilB complex. Indeed, as can be seen on Fig. S14, the predicted R_1 and R_2 parameters exhibit a different level according to their location in the protein sequence. It is noteworthy that the values associated with SilF are similar to the ones associated with the N terminus of SilB and significantly different from the rest of SilB. Thus, the fact that the relaxation parameters associated with SilF when bound to SilB does not reflect the total molecular weight of the complex is not the result of a particular bound fraction but is likely to reflect the behavior of a multidomain protein. Additionally, our observed experimental data are in very good agreement with the predicted ones. Therefore, we can conclude that the SilF/SilB complex is fully or close to be fully bounded.

SilF interacts with SilB in the presence of silver

We have demonstrated that SilF and SilB interact with each other without the presence of silver ions. Additionally, we have shown that they both bind silver ions. Therefore, we were wondering if SilF could bind SilB in the presence of silver ions. To test this hypothesis, we prepared a preformed ^{15}N-SilF/Ag^+ sample with a [SilF]/[Ag^+] ratio of 1, and we added SilB at a

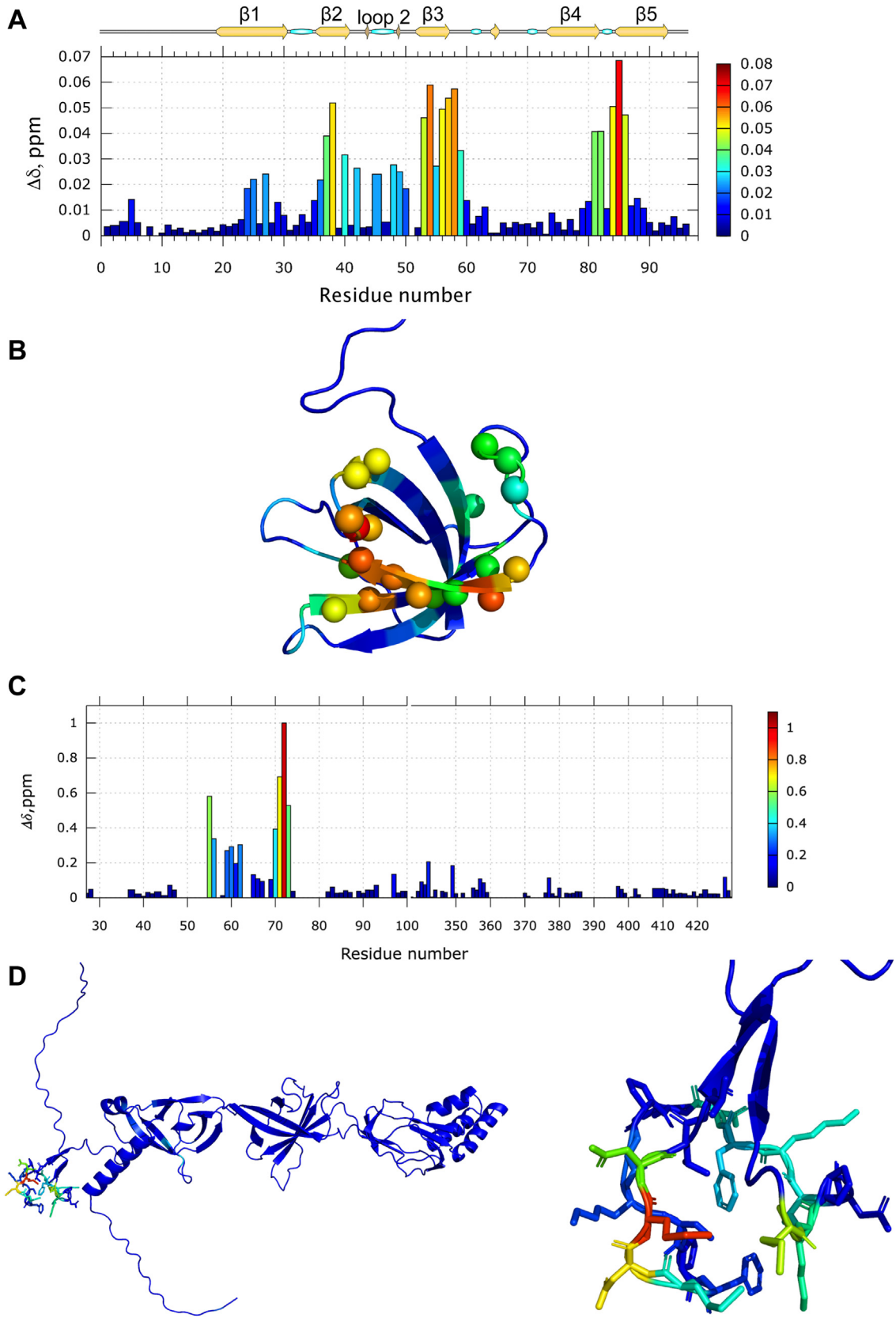

Figure 4. NMR characterization of the SilF/SilB interaction without the presence of silver ions. *A*, CSPs (Δδ) for ^{15}N-SilF in the presence of 1 equivalent of SilB as a function of the residue number. *B*, the observed CSPs in (*A*) are mapped onto the solution structure of SilF. *C*, CSPs (Δδ) for ^{15}N-SilB resonances in the presence of 1 equivalent of SilF as a function of the residue number. For a sake of clarity, the x axis is broken between residue number 100 and 340. *D*, the observed CSPs in (*C*) are mapped onto the modeled structure of the full SilB on the left and mapped on the magnified interacting region on the right. For all panels, the same color palette highlights the most significant CSPs (from *blue* to *red*). CSP, chemical shift perturbation.

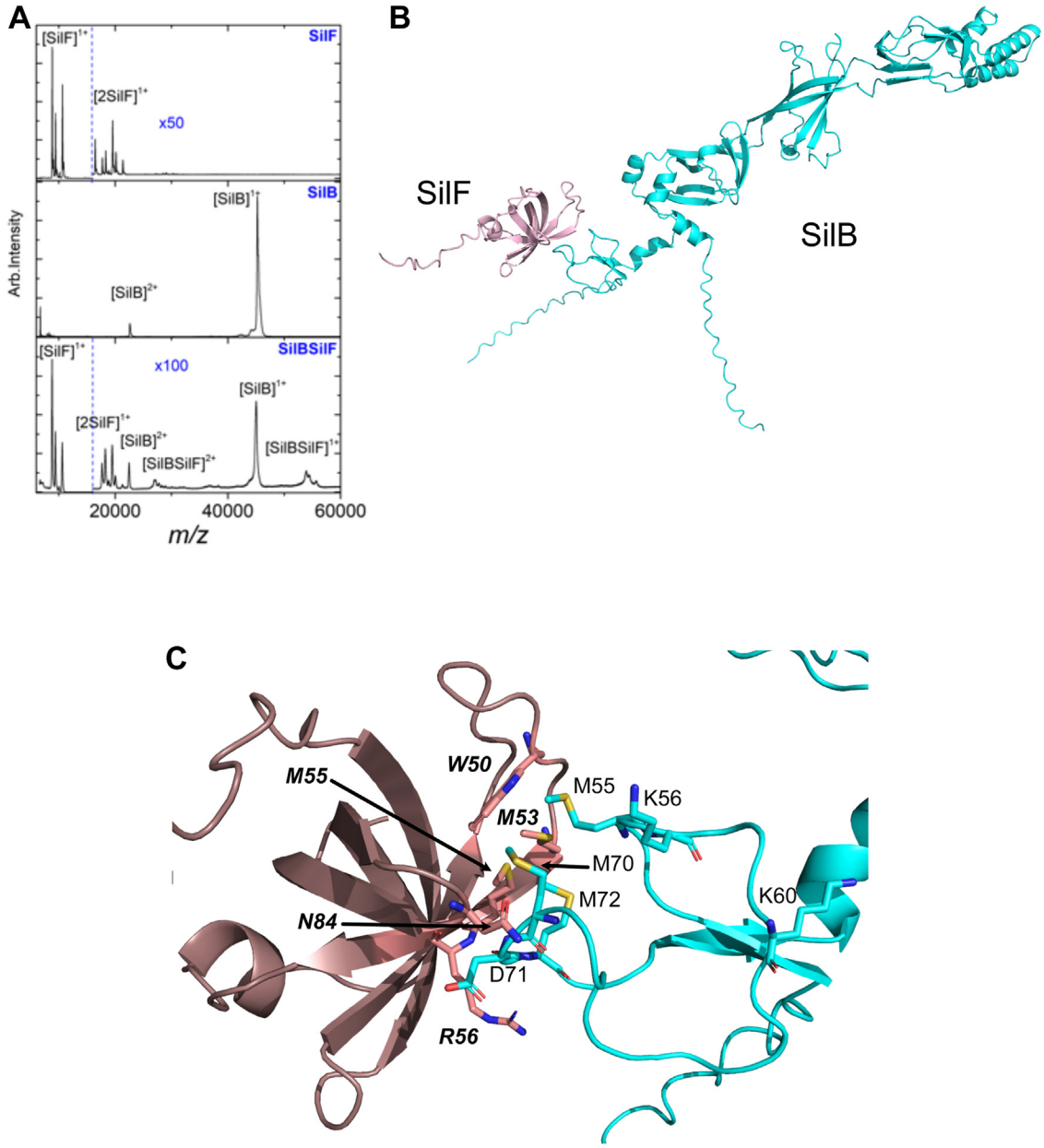

Figure 5. SilF/SilB complex. *A*, MALDI-MS spectra recorded for SilF (*top*) SilB (*middle*) and an equimolar mixture of both proteins (*bottom*). The high m/z parts of the spectra for SilF and for the mixture have been magnified. *B*, structure of the SilF/SilB complex predicted by Alphafold. *C*, the magnified view of the binding site indicates the main residues involved in the SilF/SilB complex formation.

[SilF]/[SilB] ratio of 1. We observed significant differences between the $^{1}H,^{15}N$-HSQC spectrum of ^{15}N-SilF in the presence of SilB and silver and those obtained for the ^{15}N-SilF and ^{15}N-SilF-Ag^{+} samples where the signals either shift or exhibit strong attenuation (Fig. S15*A*). A detailed analysis enables to distinguish between signals that come back to the position they occupied in the free SilF HSQC spectrum and signals that experience a change in their shift direction (Fig. 6, *A* and *B*). Residues close to the silver interaction region such as S41, A47, V48, G49, and W50 display signals that shift back to the position they occupied in the $^{1}H,^{15}N$-HSQC spectrum of the free SilF (Fig. 6*C*). This suggests a loss of interaction between these residues and Ag^{+}. Other residues such as K36, K37, I80, Q81, Q82, G83, and L88 exhibit a change of their shift direction compared to silver binding and indicates a different binding mode to SilF in presence of SilB (Fig. 6, *A*–*C*). Furthermore, various residues involved in silver interaction, such as I38, I40, H42, E43, A44, I45, M53, T54, M55, R56, F57, and T58 that stretch along the β2 and β3 strands, show strong signal broadening (Fig. 6*A*) due to an intermediate-exchange regime. In the same order of idea, we have compared the $^{1}H,^{15}N$-HSQC spectra of (i) ^{15}N-SilB1, (ii) ^{15}N-SilB1 + 1 eq. of SilF, (iii) ^{15}N-SilB1 + 1 eq. of Ag^{+}, (iv) and ^{15}N-SilB1 + 1eq. SilF + 1eq. Ag^{+}. In the presence of 1 eq. of Ag^{+} to a preformed

Table 1
Relaxation parameters mean values R_1 and R_2 measured for the different complexes SilF/Ag^+/SilB

Samples	R_1, s^{-1}	R_2, s^{-1}
^{15}N-SilF	1.72 ± 0.10	7.8 ± 0.5
^{15}N-SilF + 1 Ag^+	1.81 ± 0.10	7.4 ± 0.7
^{15}N-SilF + 2 Ag^+	1.85 ± 0.10	7.6 ± 0.9
^{15}N-SilF + SilB	1.47 ± 0.12	19.8 ± 2.0
^{15}N-SilF + 1 Ag^+ + SilB	1.34 ± 0.12	19.2 ± 2.7
^{15}N-SilF + 1 Ag^+ + SilB + 1 Ag^+	1.61 ± 0.10	13.0 ± 0.9
^{15}N-SilF + 1 Ag^+ + SilB + 2 Ag^+	1.63 ± 0.11	13.4 ± 0.9

The mean values were obtained from averaging relaxation parameters by considering residues involved in only structured part of SilF. The error values were deduced using the standard deviation.

SilB1/SilF complex (Fig. 6*D*), the signals of residues close to the silver interaction region such as K60 or G65 are displaced to an intermediate position (#4 in Fig. 6*D*) between the position they occupied in the ^{1}H,^{15}N-HSQC spectrum of the free SilB1 (#1 in Fig. 6*D*) and SilB1 + 1 eq. Ag^+ (#3,3′ in Fig. 6*D*). This observation supports the formation of an intermediate shared complex.

To confirm the presence of the SilF–Ag^+–SilB complex, we carried out relaxation experiments to quantify longitudinal and transverse ^{15}N relaxation rates. The corresponding R_1 and R_2 values for the SilF–Ag^+–SilB complex give 1.34 ± 0.12 and 19.2 ± 2.7 s^{-1}, respectively, and are similar to the measured relaxation rates of the SilF + SilB sample and thus presents a fully or close to fully bounded complex.

To further investigate the silver binding onto SilF in the presence of SilB, we prepared a preformed ^{15}N-SilF/SilB sample with a [SilF]/[SilB] ratio of 1 and gradually added a silver ion solution ranging from 0.1 to 2 equivalents. As observed for the ^{15}N-SilF + 1eq. Ag^+ + 1eq. SilB sample, some residues displayed strong signal attenuation until 1.3 eq. of silver (Fig. S15*B*). To derive the dissociation constant (K_d) and the dissociation rate (k_{off}) of the 1:1 SilF-SilB:Ag^+ equilibrium, we used NMR lineshape analysis using TITAN(19). Here, we report an average K_d of 33 ± 7 μM and average k_{off} = 198 ± 27 s^{-1}. While we obtained a similar K_d value for the SilF/Ag^+ equilibrium, the dissociation rate has increased by a factor of eight and support the fact that the silver ion environment is quickly remodeled toward the formation of a SilF-Ag^+-SilB binding intermediate, where the silver ion is shared between SilF and SilB. The association rate (k_{on}) is 6.10^6 M^{-1} s^{-1}, in the same order of magnitude compared to the formation of the intermediate complex CusF–Ag^+–CusB (17), and suggests a first step with a quick association of SilF, Ag^+, and SilB. To understand the effect of an increase of the silver concentration in the cell, we added another eq. of silver ions to the current ^{15}NSilF–Ag–SilB complex (*i.e.*, [Ag^+]/[SilF] = 2 and [Ag^+]/[SilB] = 2). At this point, we observed that (i) the signal intensities in the spectrum are comparable to their intensities in the ^{15}N-SilF + 1Ag^+ spectrum (Fig. S15*B*); (ii) the signals shift back to the position they occupied in the ^{15}N-SilF + 1Ag^+ spectrum (Fig. S15*C*); and (iii) the values of the longitudinal (R_1) and transverse (R_2) relaxation parameters shift back to the values for the ^{15}N-SilF + 1Ag^+ complex (Table 1). Adding a third equivalent of Ag^+ does not change the intensities of the signals nor the chemical shifts and relaxation parameters values (Table 1). These results clearly indicate that (i) the presence of 2 or 3 eq. of silver ions induces a mixture of a predominant ^{15}N-SilF+Ag^+ complex with a small amount of ^{15}N-SilF–Ag^+–SilB complex and that (ii) an increase of the level of silver ions in the cell would destabilize the formation of the SilF–Ag^+–SilB complex. Thus, one may wonder how gram-negative bacteria may keep the optimum-bound fraction of the SilF–Ag^+–SilB complex despite a high level of silver concentration in the periplasm?

Interplay between SilF, SilB, and SilE

To answer this question, we were seeking to understand whether SilE functions as a relay protein responsible for delivering silver ions directly to SilF or SilB. Until now, SilE has been identified as a regulator protein that prevents silver ions to overload the cell. To test whether SilE interacts with SilF, we recorded ^{1}H-^{15}N HSQC experiments on a ^{15}N-SilE sample either in its free form or in the presence of SilF at a [SilF]/[SilE] ratio of 2. As evidenced by Fig. S16*A*, the two spectra perfectly overlap, demonstrating that SilF and SilE do not interact. To the latter sample, we then added Ag^+ at a [Ag^+]/[SilE] ratio of 2 (Fig. S16*B*), and the two spectra perfectly overlap. To complement these series of experiments, we have started from a preformed ^{15}N-SilE + 4 Ag^+ sample and have added 2 eq. of SilF. As can be seen on Fig. S16*C* the final HSQC spectrum nicely overlaps with the HSQC spectrum of a ^{15}N-SilE + 2Ag^+ spectrum. Moreover, we achieved the reverse experiment and added SilE to a solution of ^{15}N-SilF preloaded with 1 eq. of silver ions. The recorded ^{1}H-^{15}N HSQC spectra before and after the addition of SilE are strictly similar (Fig. S16*D*). These results demonstrate that (i) SilE and SilF do not interact with each other regardless of the presence of silver ions, and (ii) SilE does not compete with SilF for silver binding likely because SilF has a much higher affinity for silver ions compared to SilE. Therefore, SilE is not a relay protein for SilF and is not involved in a mechanism of silver transfer to SilB.

Thus, we have tested whether SilE directly interacts with SilB and bypasses SilF by adding SilB on a ^{15}N-SilE sample at a [SilB]/[SilF] = 1.3. We have recorded a ^{1}H-^{15}N HSQC spectrum before and after the addition of SilB. In the same order of idea, we have also recorded a spectrum where we have added silver at a [Ag^+]/[SilB] = 1 on the previous SilE + SilB sample. For both experiments (Fig. S16, *E* and *F*), we did not observe any change in the spectra. In the same order of idea, we started from a preformed ^{15}N-SilE + 6Ag^+ sample and progressively added 0.65 eq. then 1.3 eq. of SilB1. Fig. S16*G* shows that the signals of the residues of SilE involved in the interaction such as A57 and G58 shift back to the position they occupied for the free SilE. These insightful results evidence that SilE does not interact with SilB regardless of the presence of silver ions. These observations support the fact that SilF or SilB have a better affinity for silver ions compared to SilE. All together, these results demonstrate that SilE more likely plays the role of a silver regulator by sequestrating the extra silver ions, keeping the SilF–Ag^+–SilB complex to its optimum-bound fraction.

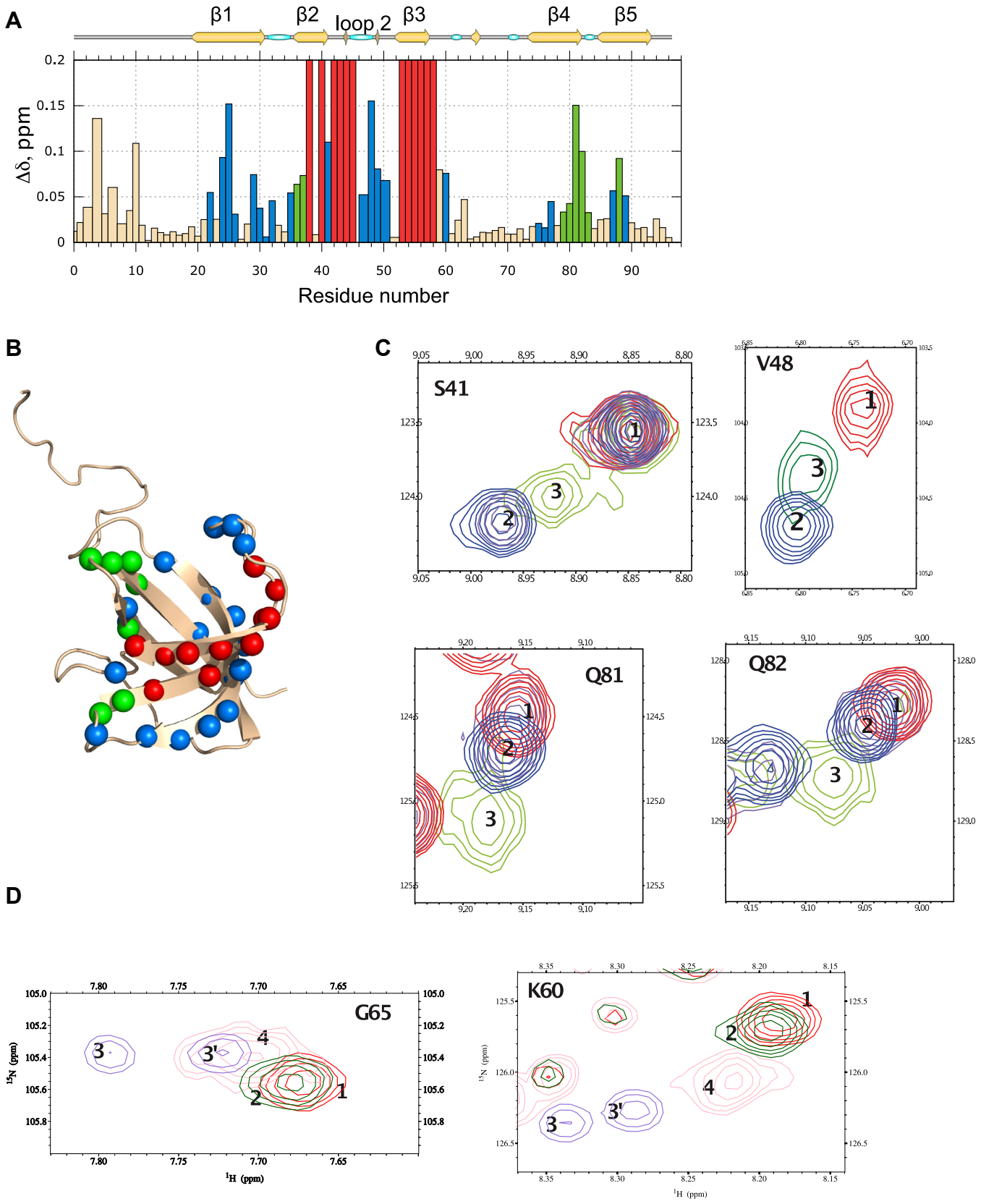

Figure 6. Interaction SilF/Ag^{+}/SilB. *A*, CSPs of ^{15}N-SilF resonances in the presence of 1 equivalent of silver ion and 1 equivalent of SilB. *Red bars* highlight the residues that disappeared, *blue bars* correspond to residues that shifted back to the position they occupied in the HSQC spectrum of ^{15}N-SilF, and *green bars* indicate the residues that modified their shift directions compared to Ag^{+} binding. *B*, mapping of the CSPs obtained in (*A*) on the 3D structure of SilF in the presence of 1 eq. of both Ag^{+} and SilB. The same color palette is used as defined in (*A*). *C*, overlay of ^{1}H-^{15}N HSQC spectra of ^{15}N-SilF (*red*, 1), ^{15}N-SilF + 1 Ag^{+} (*blue*, 2), and ^{15}N-SilF + 1 Ag^{+}+ SilB (*green*, 3) for top panel residues with a related HSQC peak that come back to the position they occupied in SilF HSQC

Discussion

To date, the sil efflux system and its silver resistance mechanism has been largely overlooked, likely because of the progress made on its homologous Cus system. Although the SilFBCA proteins share almost 80% sequence identity with the Cus operon homolog proteins, the two systems also display discrepancies that we have emphasized in the present study. For the sake of comparison, we solved the structure of the free form of SilF and the Ag^+-bound SilF. The silver ion did not perturb the structural organization of SilF which keeps a similar fold in both cases. Silver ions interact with SilF through a network of two methionines and one histidine similarly to its counterpart CusF (10) and display a dissociation constant of 9.5 ± 3.5 μM with a dissociation rate of 25.4 ± 4.5 s^{-1}. From its side, the periplasmic component of the efflux pump SilB binds silver ions in a region that spans M55 to F73 and a second one located in the highly flexible C terminus. For the first binding site, NMR signals show either a strong signal attenuation or two distinct chemical shifts due to the possible presence of two conformations. Whether we refer to CusB or SilB of *C. metallidurans* CH34, the residues that belong to the interacting region are mainly conserved (Fig. S7*B*). Thus, it is likely that the structure adopted by the N terminus of SilB is comparable to the one adopted by CH34 or CusB. In light of the present results, one may wonder whether the cus and the sil systems may behave differently to remove metal ions from the cell. Conversely to what has been shown for the cus system, our results clearly demonstrate that SilF and SilB interact without the presence of silver ions and involve (i) a different more extended binding interface or (ii) a different dynamical regime compared to what they experience when they individually bind Ag(I). It is also noteworthy that CSPs induced on both side of the complex are in the fast exchange regime, reflecting a weaker binding compared to their individual silver binding. Furthermore, SilF mainly binds SilB through an ensemble of hydrophobic residues (I38, M53, F57, and I85) associated with positively charged residues (K37 and R56) (Fig. S4*A*). From its side, SilB interacts with SilF through a surface that overlaps the one seen when SilB interacts with silver. This interface mainly involves a network of hydrophobic residues (M55, F61, M70, and M72) associated with negatively charged residues (D62, D71, and D73) (Fig. S7*B*). CSPs mapping is in fact in good agreement with the SilF/SilB model and the exposed electrostatic surfaces (see Fig. S17), while the residues of SilF and SilB involved in the interaction are highly conserved in CusF and CusB (see Figs. S4*A* and S7*B*). Additionally, we have shown that the SilF binding to SilB significantly increases the silver dissociation rate by a factor of eight compared to that of SilF alone. According to these results, it is possible to compare the half-life of the Ag^+/SilF complex that is 28 ms, when SilB is not present and decreases to 3.5 ms when SilB binds SilF (26, 27) and suggest the quick formation of an intermediate complex that occurs in a two-step process with SilF and SilB that are initially prepositioned to host a silver ion. Further addition of silver ions would dissociate partially the formed complex.

To the best of our knowledge, this two-step process only occurs in the sil system while the counterparts CusF and CusB only bind in the presence of Cu(I) or Ag(I). Therefore, it has encouraged us to reassess the mechanism by which silver is further evicted from the cell by referring to our current knowledge on CusF, CusB, and CusA. Recently, it has been concluded that the main signal that triggers silver eviction is based on a switch model rather than a funnel model (28, 29). This model has also been motivated by the fact that neither CusF nor CusB are capable of transferring silver ions to CusA when they are working alone (28). In this representation, CusA is a homotrimer that directs metal ions to CusC by means of charged residues complemented by a network and cluster of methionines (12, 30). While metal ions are prone to enter CusA *via* the periplasmic cleft or the cytoplasm, CusB probably harnesses its plasticity to induce different steps of CusA conformational changes that drive the passage of metal ions (13). Since SilA and CusA exhibit an 87% sequence identity (Fig. S18), it is likely that the different opening states seen in the case of CusA may also take place for SilA. Thus, one may wonder "why SilF binds SilB without the presence of silver ions and what is the advantage of such a two-step process?". To address this question, we have to recall that the deletion of *silabc* causes a loss of resistance while the deletion of *silf* does not completely abolish resistance except in a *cus*-negative background (6). This result, combined with our findings led us to hypothesize that SilF kinetically favors the formation of a SilF–Ag^+–SilB intermediate complex that activates the on-switch for SilA, a process designed for a quick answer to silver overload of the cell. With such a structural organization, the SilAB complex may bind up to six SilF (Fig. 7). SilF would function like a lever to first release the C terminus of SilB from SilA and further loosen SilA for a possible conformational change and silver extrusion. This is a plausible hypothesis if one refers to CusB, which undergoes a more compact structure upon silver binding and further induces the CusA channel opening (31). Furthermore, one may still wonder whether SilE only induces silver sequestration or may directly bind to SilB *via* SilF. This question arises from the fact that SilE can bind six silver ions (7) similarly to the SilB hexamer structure that may bind up to six SilF. The results of our experiments demonstrate that SilE does not bind to neither SilF nor SilB and that its binding affinity for silver is weaker compared to the affinity of silver for SilF and SilB. As a consequence and to the light of our results, we can conclude that SilE functions as a silver regulator protein that prevents an overload of the cell and ensures an optimal functioning of the SilF–Ag^+–SilB complex. Moreover, when the silver ions concentration turns back to a lower concentration, SilF and SilB still bind Ag^+ despite the presence of SilE and ensure that the efflux pump

spectrum and (*B*) for residues with related HSQC peak that change their shift direction in presence of SilB. *D*, overlay of ^{1}H-^{15}N HSQC spectra of ^{15}N-SilB1 (*red*, 1), ^{15}N-SilB1 + SilF (*green*, 2), ^{15}N-SilB1 + 1 Ag^+ (*purple*, 3, 3′), and ^{15}N-SilB1 + SilF + 1 Ag^+ (*pink*, 4). CSP, chemical shift perturbation; HSQC, heteronuclear single quantum coherence.

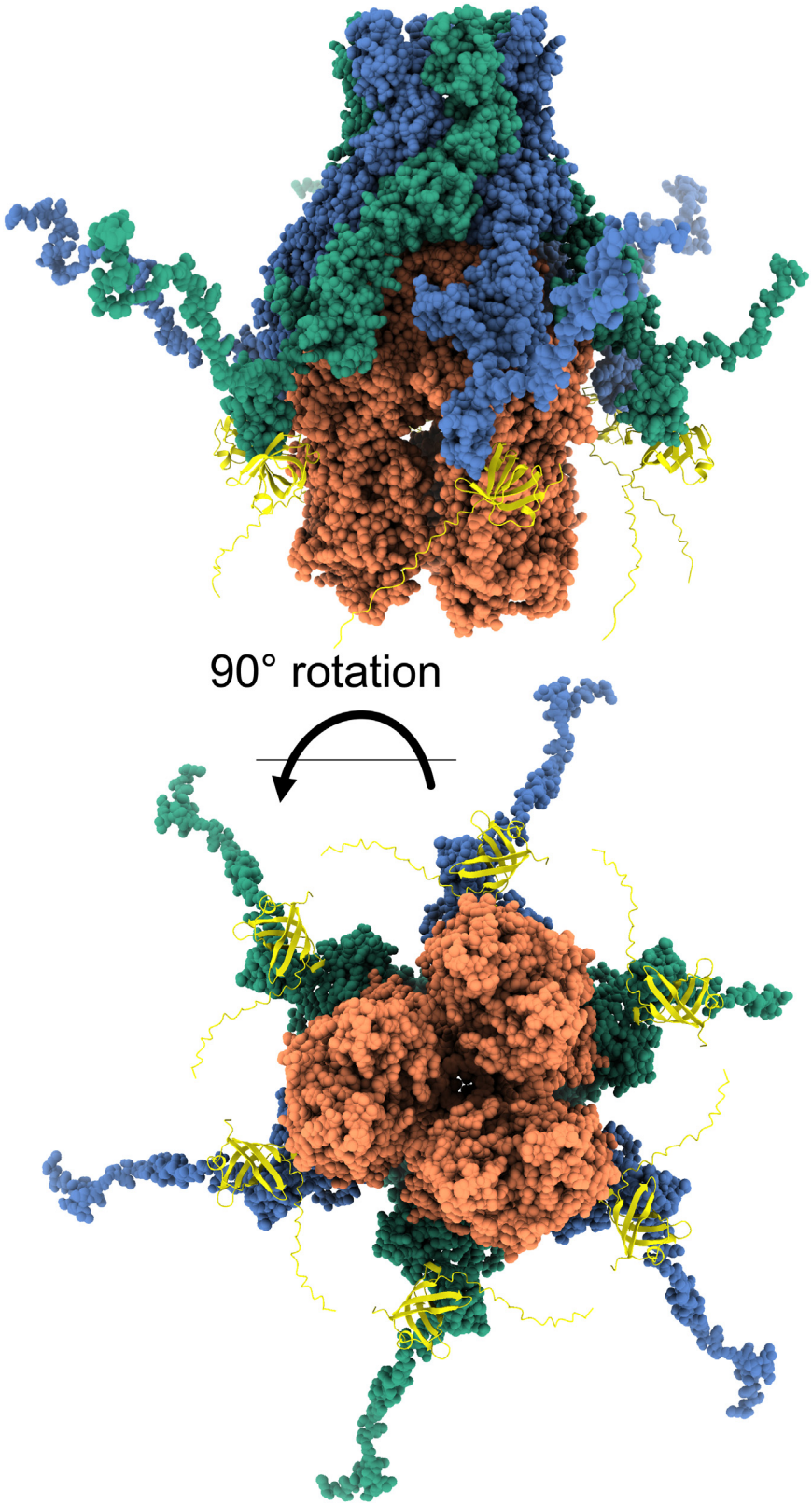

Figure 7. Putative structural arrangement of the SilA/SilB/SilF complex. Hypothetical structural arrangement of the SilA, SilB, and SilF complex. SilB is a hexamer (displayed in *blue* and *green*). SilA is a trimer (displayed in *orange*). Six molecules of SilF (displayed in *yellow*) can interact with the 6-mer of SilB (displayed in *yellow*). A rotation of 90° allows to observe the funnel for silver extrusion through the methionine relay network of SilA.

does not stop working. These last observations complements the study published by Randall *et al.* (6) who wondered whether SilE might act as a chaperone for SilB.

Experimental procedures

Protein expression and purification

The different protein constructs (SilF, SilB, and SilB1) in pEtM-60 (Novagen) were expressed with their N terminus fused to NusA and a hexa histidine tag (His6 tag). The *Escherichia Coli* BL21 Gold (DE3) were transformed with those plasmids for overexpression. Cells were grown either in LB medium with 50 mg/L kanamycin or for uniform isotopic labeling, in M9 medium supplemented with 1 mM $MgSO_4$, 0.1 mM $CaCl_2$, 4 g/L D-glucose, 6 mg/L thiamine, 50 mg/L kanamycin, 1 % (vol/vol) trace element solution [5 g/L EDTA, 0.5 g/L $FeCl_3$, $6H_2O$, 5 mg/L ZnO, 1 mg/L $CuCl_2$, $2H_2O$, 1 mg/L Co $(NO_3)_2$, $6H_2O$ and 1 mg/L $(NH_4)_6Mo_7O_{24}$, $4H_2O$], and 1 g/L $^{15}NH_4Cl$ as main nitrogen source. For ^{13}C-labeled protein $^{12}C_6$-D-glucose was replaced by 2.5 g/L $^{13}C_6$-D-glucose. For ^{2}H-labeled protein, a first preculture of 25 ml in LB in distilled water in presence of kanamycin and a second preculture of 25 ml in LB in D_2O supplemented by kanamycin are fulfilled. Finally, the last preculture is prepared in M9 medium in D_2O and kanamycin. The same procedure is used for the culture except for the use of D_2O instead of distilled water.

The cells were grown at 37 °C until A_{600} reached 0.6 to 0.8, and the expression was induced by adding 1 mM IPTG. Induction was performed for 3 to 4 h at 37 °C. The cells were lysed in 50 mM Tris-base, 300 mM NaCl, and 5 mM imidazole at pH 7.8 to 8. The clarified cell lysate was loaded on Ni-NTA Superflow column (Qiagen), equilibrated with 50 mM Tris-base, 300 mM NaCl, 5 mM imidazole, and 1 % (vol/vol) glycerol at pH 7.8 to 8. The bound protein was eluted by applying an imidazole gradient. NusA and His6 tags were removed by cleavage with the tobacco etch virus protease at 5 °C overnight while dialyzed against lysis buffer containing 50 mM Tris-base, 300 mM NaCl, 5 mM β-Me, and 5 mM imidazole at pH 7.8 to 8. Proteins are separated from NusA-His6 by second Ni^{2+} affinity chromatography using as a first step elution with 10% of solution (50 mM Tris-base, 300 mM NaCl, 500 mM imidazole, 1 % (vol/vol) glycerol and pH 7.8–8) and then a gradient elution. To obtain an improved purity, we performed size-exclusion chromatography using a Superdex 75 16/600 column (GE Healthcare) in 20 mM MES and 20 mM NaF at pH 6.8.

NMR experiments

All the NMR samples were prepared in 20 mM MES buffer and 20 mM NaF (pH 6.8) complemented by 10 % D_2O.

The ^{1}H, ^{13}C, ^{15}N NMR signal assignment of SilF has been achieved using the conventional 2D and 3D experiments recording at 293 K and at a proton Larmor frequency of 600 MHz (14.1 T) with a Bruker Avance III spectrometer equipped with warm TCI probe on a double labeled sample (U-[^{13}C,^{15}N]). The following set of NMR experiments were used: 2D [^{15}N,^{1}H]-HSQC, 2D aliphatic [^{13}C,^{1}H]-HSQC, 2D aromatic [^{13}C,^{1}H]-Sofast-HMQC (32) as reference spectra; the bidirectional and sequential experiments 3D HNCACB, 3D CBCA(CO)NH, 3D HNCA, 3D HN(CO)CA, 3D HNCO, and 3D HBHA(CO)NH for the backbone assignment; 3D [^{1}H]-TOCSY-[^{1}H,^{15}N]-HSQC, 3D [^{1}H,^{13} C,^{1}H]-TOCSY, and 3D [^{13}C,^{13} C,^{1}H]-TOCSY for side chain assignment. Aromatic ^{13} C and ^{1}H assignment has been achieved thanks by the 2D [^{1}H,^{1}H]-TOCSY recording on SilF, labeled at the natural abundance. Methionine CH3ε were assigned using observed NOEs with surrounding hydrogens in the 3D [^{1}H]-nuclear overhauser effect spectroscopy-[^{1}H,^{13} C]-HSQC. The [^{13}C,^{15}N]-labeled $SilF^{[1-96]}$ samples were concentrated at 500 μM. The $SilF^{[1-96]}$ samples at natural abundance, either bound to or free of silver ion, were concentrated at 300 μM. For the NMR analysis of the Ag^{+}-bound SilF, 1:1 equivalent of the silver ions was added to the solution.

Concerning SilB and SilB1, NMR experiments were carried out at 293K with a spectrometer Bruker NEO operated at a ^{1}H frequency of 900 MHz (21.1 T) and equipped with a triple HCN cryoprobe. The backbone resonance assignments of SilB1 have been performed using a combination of the classical 3D experiments: 3D HNCACB, 3D CBCA(CO)NH, 3D HNCA, 3D HN(CO)CA, and 3D HNCO.

The interaction studies have been carried out using CSP measurement, where a series of ^{1}H-^{15}N HSQC were recorded for a protein while adding gradually a small volume of the concentrated silver solution ($AgNO_3$) until reaching saturation. The combined CSP is calculated using the following equation:

$$\Delta\delta = \sqrt{(\Delta\delta_H)^2 + \left(\Delta\delta_N/5\right)^2}$$

Where $\Delta\delta_H$ are the CSPs in the proton dimension and $\Delta\delta_N$ are the CSPs in the nitrogen dimension. The calculation of kinetic and thermodynamic parameters k_{off} and K_d has been conducted by following the protocol provided by Waudby *et al.* (19). This article clearly describes the different steps to prepare the sample, record the experiments, and to analyze the NMR titration data using their dedicated software named TITAN. The current software is running under Matlab (The MathWorks, Inc), and different binding models are implemented while the fitted parameters are deduced from 2D lineshape analysis. Here, we used a two-states model to describe the binding between the different partners.

Relaxation experiments including ^{15}N longitudinal (R_1) and transversal (R_2) relaxation as well as the ^{1}H-^{15}N heteronuclear cross-relaxation rates were performed on the following samples: ^{15}N-SilF, ^{15}N-SilF + 1 Ag^{+}, ^{15}N-SilF + 2 Ag^{+}, ^{15}N-SilF + SilB, and ^{15}N-SilF + SilB + 1 Ag^{+}. For the R_1 experiments, we used relaxation delays ranging from 40 to 2000 ms were used with a recycling delay of 3.5 s. In the case of the R_2 experiments, we used relaxation delays ranging from 8 to 480 ms were used with a recycling delay of 3.5 s. For ^{1}H-^{15}N heteronuclear NOE experiments, 2D spectra were recorded with and

without pre-saturation of amide protons. The relaxation delay was set to 4.5 s to allow the bulk water magnetization to return as close as possible to the equilibrium state.

De novo *structure calculations of the free SilF and the 1:1 SilF:Ag$^+$ complex*

The structures of both bound and free states of SilF$^{[1-96]}$ were determined using a set of distances, dihedral angles, and H-bonds constraints. The distance constraints were derived from NOEs recorded with two 3D, either ^{13}C- or ^{15}N-edited, NOESY-HSQC experiments. To gain into sensitivity, the NOESY experiments on Ag-bound SilF sample were recorded with a Varian spectrometer at ^{1}H frequency 600 MHz equipped with a cryoprobe, whereas NOESY experiments on apo-SilF were recorded with a Bruker spectrometer at ^{1}H frequency 600 MHz equipped with a warm probe. Hence, we detected 1787 without a cryoprobe and 3402 NOE peaks with a cryoprobe for the free and bound states, respectively. The backbone dihedral angles (Φ,Φ) were predicted using the backbone chemical shifts and the Talos+ algorithm (https://spin.niddk.nih.gov/bax/nmrserver/talos/) (33) from the backbone chemical shifts. Some χ_1 and χ_2 side chain dihedral angles were defined according to the surrounding NOEs, but only for side chains located in the protein core. Hydrogen bonds were defined as a set of distance constraints only when they were supported by the observation of specific NOE patterns and the presence of the relevant secondary structures. Ambiguous NOE assignments and structure calculation were performed using CYANA (34), and further refinement of the protein structure geometry was carried out in presence of water molecules using a CNS water refinement script (35). In the case of Ag$^+$-bound SilF$^{[1-96]}$ structure resolution, we defined an artificial histidine residue containing the silver ion was defined. The geometry of this artificial residue was defined based on the known coordination of the silver ion with the electronic doublet of the imidazole Nδ_1 (Ag$^+$ within the imidazole plane and the coordination bond between H42 Nε_2 and Ag$^+$ set to 2.3 Å). The structure of the Ag$^+$-bound SilF homolog, CusF (PDB id. 2VB3), was used to define the coordination geometry of the silver-bound state of SilF.

Mass spectrometry experiments

For mass spectrometry, a buffer exchange was first performed on the purified protein solutions, using 5 ml individual dialyzer tubes, MWCO 3500 (Roth) in order to obtain 20 μmol L^{-1} protein solutions in ammonium acetate buffer (50 mM L^{-1}). As the matrix for MALDI experiments, we used a 20 mg mL^{-1} solution of synapinic acid in a mixture of water and acetonitrile (1:1 vol) with 0.1% trifluoroacetic acid. This solution was then mixed with protein samples (1:1 vol) before deposition on a ground steel plate. Three spots of each solution were deposited on the plate. An equimolar mixture SilB/SilF was prepared right before deposition from the pure protein solutions. For calibration, bovine serum albumine (BSA) was also deposited on the same plate with the same matrix. Mass spectra were recorded on a MALDI-TOF mass spectrometer (Ultraflextreme) in the positive ion mode and using the linear TOF configuration. Mass calibration was done using BSA monomer, dimer, and doubly charged monomer ions. For all experiments, the laser power was set to 95%. All chemicals for sample preparation were purchased from Sigma Aldrich. The mass spectra were extracted using the FlexAnalysis software (Bruker) and plotted using Origin 2016.

Alphafold modeling

To model a putative silver-bound SilB structure, we used the ColabFold server (20), which is based on the AlphaFold 2 prediction protocol (21). The sequence of SilB is given by the UniProt accession number Q9ZHD0. The modeled structures were ranked according to a quality factor issued by AlphaFold, which is a per-residue confidence metric called the plDDT, ranging from 0 to 100. The plDDT metric estimates how well the prediction would agree with an experimental structure based on the local distance difference test Cα (36). A plDDT <50 should not be interpreted except as a possible disorder prediction while a cutoff of plDDT >70 corresponds to a likely correct backbone prediction (22). It is well-calibrated, and full details on how the plDDT is produced are given in the supplementary information of the AlphaFold paper (21).

Theoretical prediction of the relaxation parameters

The predicted relaxation parameters for the SilF/SilB complex were obtained by means of the SpinRelax program (37). The analysis was performed on a set of 18 trajectories of 100 ns for a total of 1.8 μs. The different trajectories were extracted from different molecular dynamics running the ACEMD software (38). Each of the trajectories were started with the rank1 structure of the SilF/SilB complex obtained with AlphaFold. The complex was set in a cubic box by applying a 1.2 nm buffer to the protein coordinates, filled with water molecules and the specific counterions. Energy minimization was run for 2000 steps, followed by NVT equilibration for 600 ps with a time step of 2 fs and concluded with NPT equilibration in two steps: first with constraints during 3 ns and second without constraints for 3 ns. We used a Langevin's thermostat with dumping of 1 ps and Berendsen's barostat with pressure relaxation time of 800 ps. The Coulomb's electrostatic was described by the PME method with cutoff at 0.9 nm and grid spacing of 0.1 nm, whereas the van der Waals forces were described by a switching function with a cutoff at 0.75 nm. The 100 ns runs were carried out in an NVT ensemble. For this specific case, we have produced 18 quasi-independent trajectories, by generating new sets of velocity at start-up. The spinrelax program can be obtained free of charge at this address: https://github.com/zharmad/SpinRelax.

Data availability

The 20 lowest energy structures are deposited into the Protein Data Bank (PDB) identifiers 8BXJ and 8C2Q for the free and Ag-bound SilF$^{[1-96]}$, respectively. Moreover, ^{1}H, ^{15}N, and ^{13}C chemical shifts of free and Ag-bound SilF have been

deposited into Biological Magnetic Resonance Bank identifiers 34779 and 51726, respectively.

Supporting information—This article contains supporting information.

Acknowledgments—Financial support from the IR INFRANALYTICS FR2054 for conducting the research is gratefully acknowledged. The 900 MHz NMR experiments have been performed at IMEC-IS-UCCS Lille.

Author contributions—M. H. and O. W. conceptualization; M. H. and O. W. writing–original draft; M. H., C. A., Y. R. M., M. M., F.-X. C., E. B., F. C., C. C. Z., and O. W. writing–review and editing; M. H. supervision; M. H., C. A., Y. R. M., M. M., F.-X. C., E. B., F. C., and C. C. Z. investigation; M. H. and O. W. visualization; M. H., C. A., Y. R. M., M. M., F.-X. C., E. B., F. C., and C. C. Z. formal analyses; C. A., Y. R. M., M. M., E. B., and C. C. Z. validation.

Funding and additional information—This work was supported by the CNRS through the MITI interdisciplinary program Metallomix and the French ANR "Resist2silver" (grant # ANR-22-CE11-00-01).

Conflict of interest—The authors declare that they have no conflicts of interest with the contents of this article.

Abbreviations—The abbreviations used are: BSA, Bovine Serum Albumine; CSP, Chemical Shift Perturbation; HSQC, Heteronuclear Single Quantum Coherence; MALDI-TOF, Matrix-Assisted Laser Desorption/Ionization Time-Of-Flight; NOE, Nuclear Overhauser Effect; NOESY, Nuclear Overhauser Effect Spectroscopy; plDDT, predicted local Distance Difference Test; RMSD, Root Mean Square Deviation; TROSY, Transverse Relaxation-Optimized Spectroscopy.

References

1. Medici, S., Peana, M., Nurchi, V. M., and Zoroddu, M. A. (2019) Medical uses of silver: history, myths, and scientific evidence. *J. Med. Chem.* **62**, 5923–5943
2. Barras, F., Aussel, L., and Ezraty, B. (2018) Silver and antibiotic, new facts to an old story. *Antibiotics* **7**, 79
3. Mohamed, D. S., Abd El-Baky, R. M., Sandle, T., Mandour, S. A., and Ahmed, E. F. (2020) Antimicrobial activity of silver-treated bacteria against other multi-drug resistant pathogens in their environment. *Antibiotics* **9**, 181
4. McHugh, G. L., Moellering, R. C., Hopkins, C. C., and Swartz, M. N. (1975) Salmonella typhimurium resistant to silver nitrate, chloramphenicol, and ampicillin. *Lancet* **1**, 235–240
5. Gupta, A., Matsui, K., Lo, J.-F., and Silver, S. (1999) Molecular basis for resistance to silver cations in Salmonella. *Nat. Med.* **5**, 183–188
6. Randall, C. P., Gupta, A., Jackson, N., Busse, D., and O'Neill, A. J. (2015) Silver resistance in Gram-negative bacteria: a dissection of endogenous and exogenous mechanisms. *J. Antimicrob. Chemother.* **70**, 1037–1046
7. Monneau, Y., Arrault, C., Duroux, C., Martin, M., Chirot, F., Mac Aleese, L., *et al.* (2023) Structural and dynamical insights into SilE silver binding from combined analytical probes. *Phys. Chem. Chem. Phys.* **25**, 3061–3071
8. Bersch, B., Derfoufi, K. M., De Angelis, F., Auquier, V., Ekende, E. N., Mergeay, M., *et al.* (2011) Structural and metal binding characterization of the C-terminal metallochaperone domain of membrane fusion protein SilB from Cupriavidus metallidurans CH34. *Biochem* **50**, 2194–2204
9. Urbina, P., Bersch, B., De Angelis, F., Derfoufi, K. M., Prevost, M., Goormaghtigh, E., *et al.* (2016) Structural and functional investigation of the Ag+/Cu+ binding domains of the periplasmic adaptor protein SilB from Cupriavidus metallidurans CH34. *Biochem* **55**, 2883–2897
10. Loftin, I. R., Franke, S., Blackburn, N. J., and McEvoy, M. M. (2007) Unusual Cu(I)/Ag(I) coordination of Escherichia coli CusF as revealed by atomic resolution crystallography and X-ray absorption spectroscopy. *Protein Sci.* **16**, 2287–2293
11. Xue, Y., Davis, A. V., Balakrishnan, G., Stasser, J. P., Staehlin, B. M., Focia, P., *et al.* (2008) Cu(I) recognition via cation-π and methionine interactions in CusF. *Nat. Chem. Biol.* **4**, 107–109
12. Long, F., Su, C. C., Zimmermann, M. T., Boyken, S. E., Rajashankar, K. R., Jernigan, R. L., *et al.* (2010) Crystal structures of the CusA efflux pump suggest methionine-mediated metal transport. *Nature* **467**, 484–488
13. Moseng, M. A., Lyu, M., Pipatpolkai, T., Glaza, P., Emerson, C. C., Stewart, P. L., *et al.* (2021) Cryo-EM structures of CusA reveal a mechanism of metal-ion export. *mBio* **12**, e00452-21
14. Mealman, T. D., Zhou, M., Affandi, T., Chacón, K. N., Aranguren, M. E., Blackburn, N. J., *et al.* (2012) N-terminal region of CusB is sufficient for metal binding and metal transfer with the metallochaperone CusF. *Biochem* **51**, 6767–6775
15. Bagai, I., Liu, W., Rensing, C., Blackburn, N. J., and McEvoy, M. M. (2007) Substrate-linked conformational change in the periplasmic component of a Cu(I)/Ag(I) efflux system. *J. Biol. Chem.* **282**, 35695–35702
16. Bagai, I., Rensing, C., Blackburn, N. J., and McEvoy, M. M. (2008) Direct metal transfer between periplasmic proteins identifies a bacterial copper chaperone. *Biochem* **47**, 11408–11414
17. Chacón, K. N., Perkins, J., Mathe, Z., Alwan, K., Ho, E. N., Ucisik, M. N., *et al.* (2018) Trapping intermediates in metal transfer reactions of the CusCBAF export pump of Escherichia coli. *Commun. Biol.* **1**, 192
18. Loftin, I. R., Franke, S., Roberts, S. A., Weichsel, A., Héroux, A., Montfort, W. R., *et al.* (2005) A novel copper-binding fold for the periplasmic copper resistance protein CusF. *Biochem* **44**, 10533–10540
19. Waudby, C. A., Ramos, A., Cabrita, L. D., and Christodoulou, J. (2016) Two-dimensional NMR lineshape analysis. *Sci. Rep.* **6**, 24826
20. Mirdita, M., Schütze, K., Moriwaki, Y., Heo, L., Ovchinnikov, S., and Steinegger, M. (2022) ColabFold: making protein folding accessible to all. *Nat. Met.* **19**, 679–682
21. Jumper, J., Evans, R., Pritzel, A., Green, T., Figurnov, M., Ronneberger, O., *et al.* (2021) Highly accurate protein structure prediction with AlphaFold. *Nature* **596**, 583–589
22. Tunyasuvunakool, K., Adler, J., Wu, Z., Green, T., Zielinski, M., Žídek, A., *et al.* (2021) Highly accurate protein structure prediction for the human proteome. *Nature* **596**, 590–596
23. Babel, L., Nguyen, M.-H., Mittelheisser, C., Martin, M., Fromm, K. M., Walker, O., *et al.* (2021) NMR reveals the interplay between SilE and SilB model peptides in the context of silver resistance. *Chem. Comm.* **57**, 8726–8729
24. Mealman, T. D., Bagai, I., Singh, P., Goodlett, D. R., Rensing, C., Zhou, H., *et al.* (2011) Interactions between CusF and CusB identified by NMR spectroscopy and chemical cross-linking coupled to mass spectrometry. *Biochem* **50**, 2559–2566
25. Nguyen, M.-H., Martin, M., Kim, H., Gabel, F., Walker, O., and Hologne, M. (2019) Molecular recognition of ubiquitin and Lys63-linked diubiquitin by STAM2 UIM-SH3 dual domain: the effect of its linker length and flexibility. *Sci. Rep.* **9**, 14645
26. Corzo, J. (2006) Time, the forgotten dimension of ligand binding teaching. *Biochem. Mol. Biol. Educ.* **34**, 413–416
27. Gianni, S., and Jemth, P. (2017) How fast is protein-ligand association? *Trends Biochem. Sci.* **42**, 847–849
28. Chacon, K. N., Mealman, T. D., McEvoy, M. M., and Blackburn, N. J. (2014) Tracking metal ions through a Cu/Ag efflux pump assigns the functional roles of the periplasmic proteins. *PNAS* **111**, 15373–15378
29. Kim, E. H., Nies, D. H., McEvoy, M. M., and Rensing, C. (2011) Switch or funnel: how RND-type transport systems control periplasmic metal homeostasis. *J. Bacteriol. Res.* **193**, 2381–2387
30. Su, C. C., Long, F., Lei, H. T., Bolla, J. R., Do, S. V., Rajashankar, K. R., *et al.* (2012) Charged amino acids (R83, E567, D617, E625, R669, and K678) of CusA are required for metal ion transport in the cus efflux system. *J. Mol. Biol.* **422**, 429–441

31. Meir, A., Abdelhai, A., Moskovitz, Y., and Ruthstein, S. (2017) EPR spectroscopy targets structural changes in the E. coli membrane fusion CusB upon Cu(I) binding. *Biophysical J.* **112**, 2494–2502
32. Rossi, P., Monneau, Y. R., Xia, Y. L., Ishida, Y., and Kalodimos, C. G. (2019) Toolkit for NMR studies of methyl-labeled proteins. *Methods Enzymol* **614**, 107–142
33. Shen, Y., Delaglio, F., Cornilescu, G., and Bax, A. (2009) TALOS+: a hybrid method for predicting protein backbone torsion angles from NMR chemical shifts. *J. Biomol. NMR* **44**, 213–223
34. Güntert, P., and Buchner, L. (2015) Combined automated NOE assignment and structure calculation with CYANA. *J. Biomol. NMR* **62**, 453–471
35. Brunger, A. T. (2007) Version 1.2 of the crystallography and NMR system. *Nat. Protoc.* **2**, 2728–2733
36. Mariani, V., Biasini, M., Barbato, A., and Schwede, T. (2013) lDDT: a local superposition-free score for comparing protein structures and models using distance difference tests. *Bioinformatics* **29**, 2722–2728
37. Chen, P.-C., Hologne, M., Walker, O., and Hennig, J. (2018) *Ab Initio* prediction of NMR spin relaxation parameters from molecular dynamics simulations. *J. Chem. Theor. Comput.* **14**, 1009–1019
38. Harvey, M. J., Giupponi, G., and Fabritiis, G. D. (2009) ACEMD: accelerating biomolecular dynamics in the microsecond time scale. *J. Chem. Theor. Comput.* **5**, 1632–1639